Rational design of chemical- and light-inducible cGAS activation based on mechanistic insights

Check for updates

Yiting Tang[1], Wenjuan Wang[2] & Chunlai Chen [1] ✉

Cyclic GMP-AMP synthase (cGAS) plays a pivotal role in the cGAS-STING pathway as a DNA sensor that binds to double-stranded DNA (dsDNA) and subsequently induces type I interferon expression, thereby contributing significantly to the innate immune response. Several human and viral proteins have been identified to enhance or inhibit cGAS activity. The underlying molecular basis that underpins these regulatory effects remain elusive. In this study, we employ the highly sensitive dcFCCS method to systematically examine phase separation and binding affinities among cGAS, dsDNA, and several accessory proteins. We reveal that the binding strength between cGAS and accessory proteins is the key factor to affect cGAS phase separation and enzymatic activity, which guide us to develop a chemical-inducible strategy and a light-inducible strategy to manipulate cGAS phase separation and immune signaling in test tubes and in living cells. Thus, our mechanistic insights offer guidance for manipulating multi-component phase separation systems.

Cyclic GMP-AMP synthase (cGAS) is a key intracellular pattern recognition receptor for sensing cytoplasmic DNA, an important indicator of pathogen infection[1]. Dysregulation of intracellular cGAS is strongly associated with a range of diseases[2–5]. Upon binding to dsDNA, cGAS protein undergoes a conformational change to activate its enzymatic activity to produce cGAMP, triggering an effective immune response downstream in cells[6–12]. Liquid-liquid phase separation (LLPS) of cGAS and dsDNA is essential to burst the enzymatic activity of cGAS[13,14]. To date, a number of human and viral proteins have been identified as influencing the LLPS of cGAS and dsDNA, thereby regulating the enzymatic activity of cGAS within cells[15].

Human Ras-GTPase-activating protein SH3 domain-binding protein 1 (G3BP1) and Poly(rC)-binding protein 1 (PCBP1) have been demonstrated to accelerate cGAS response to dsDNA and to enhance the activity of the cGAS by promoting cGAS oligomerization and LLPS-induced condensed phase (Fig. 1A, top)[16–18]. On the other hand, several viral tegument proteins, including Varicella-Zoster virus ORF9 (VZV-ORF9), Kaposi's sarcoma-associated herpesvirus ORF52 (KSHV-ORF52), and Herpes simplex virus type 1 VP22 (HSV1-VP22), have been demonstrated to inhibit the activity of cGAS[19–23]. These viral proteins appear to disrupt the LLPS of cGAS and dsDNA and to exclude cGAS from the condensed phase, strongly inhibiting the cGAS activity (Fig. 1A, bottom)[19–21]. At the molecular level, it remains elusive how these proteins could enhance or inhibit cGAS-dsDNA LLPS and cGAS activity. Further

mechanistic insights could guide the development of new tools to regulate protein-dsDNA LLPS in test tubes and in living cells, as well as cGAS-mediated immune responses.

In our previous studies, we have demonstrated that dual-color fluorescence cross-correlation spectroscopy (dcFCCS) is a highly sensitive quantitative tool to examine LLPS at the nanoscale in real-time and to measure binding affinities between molecules in the diluted phase, as well as in the condensed phase[24–26]. Here, we applied dcFCCS to quantitatively examine how LLPS of cGAS and dsDNA is affected by accessory proteins: G3BP1, PCBP1, ORF9, ORF52, and VP22. Interestingly, after systematically quantifying binding affinities among cGAS, dsDNA, and these accessory proteins, we pinpointed that the interaction strength between cGAS and accessory proteins is the key factor to affect LLPS and the activity of cGAS. Guided by our newly-discovered mechanistic insights, we developed chemical-inducible and light-inducible cGAS phase separation and signaling regulation systems in test tubes and in living cells.

Results

Regulation of condensate formation and enzymatic activity of cGAS by accessory proteins

Full-length cGAS was expressed, purified, and labeled with organic fluorophores[9] (Tables S1 and S2). NHS ester on fluorophore could react with primary amines without selectivity, which could affect cGAS-DNA interactions and subsequent LLPS and cGAS activity. Therefore, several

[1]State Key Laboratory of Membrane Biology, Beijing Frontier Research Center for Biological Structure, School of Life Sciences, Tsinghua University, Beijing, China. [2]Technology Center for Protein Sciences, School of Life Sciences, Tsinghua University, Beijing, China. ✉e-mail: chunlai@mail.tsinghua.edu.cn
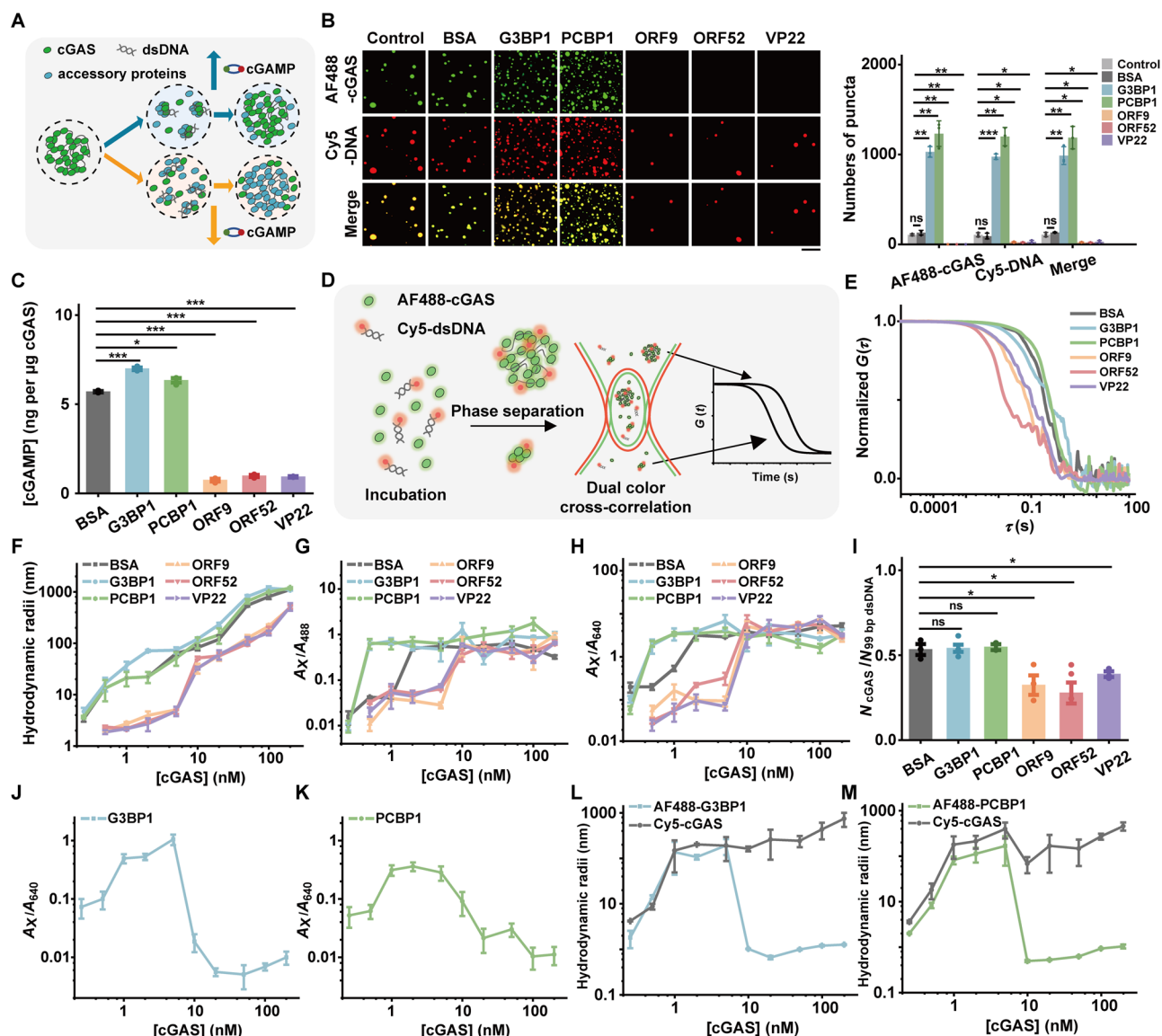
Fig. 1 | LLPS of cGAS-dsDNA affected by accessory proteins. A The scheme of accessory proteins modulating cGAS phase separation and enzymatic activity. **B** Puncta formed from cGAS, 99 bp dsDNA and accessory proteins captured by a conventional confocal fluorescence microscope. 10 μM 99 bp dsDNA was added to the mixture of equal amounts of cGAS and accessory proteins (10 μM). 10 μM BSA was used to maintain a similar protein concentration in solution. The whole images were shown in Figure S1G. Puncta numbers per field of whole images were counted. Scale bar: 5 μm. **C** The cGAMP production of 400 nM cGAS mixed with 400 nM dsDNA in the presence of 400 nM accessory proteins. **D** Schematic diagram of the dcFCCS assay. AF488-cGAS and Cy5-dsDNA diffuse randomly through the excitation volume of 488 and 640 nm lasers. Only complexes and condensates carrying both AF488-cGAS and Cy5-dsDNA contribute to cross-correlation curves, whose relaxation times correlate with their radii. **E** Normalized dcFCCS curves of condensates formed by 100 nM AF488-cGAS and 100 nM 99 bp Cy5-dsDNA with 100 nM accessory proteins. **F** Hydrodynamic radii of condensates derived from

dcFCCS curves. (**G**) A_X/A_{488} roughly estimates proportions of dsDNA participating in condensates under indicated cGAS concentrations. **H** A_X/A_{640} roughly estimating proportions of cGAS participating in condensates. **I** Stoichiometry of cGAS and dsDNA within condensates in the presence of different accessory proteins at 20 nM. **J** A_X/A_{640} roughly estimating proportions of G3BP1 participating in condensates under indicated cGAS concentrations. **K** A_X/A_{640} roughly estimates proportions of PCBP1 participating in condensates under indicated cGAS concentrations. **L** Hydrodynamic radii of particles or condensates containing G3BP1 or cGAS derived from their corresponding FCS curves. **M** Hydrodynamic radii of particles or condensates containing PCBP1 or cGAS derived from their corresponding FCS curves. Data are presented as mean ± SEM (N = 3), with individual points plotted in bar graphs. Statistical significance was assessed by two-tailed unpaired t test in (**B**, **C** and **I**). Statistical differences were represented as follows: ns not significant, *$P < 0.05$, **$P < 0.01$, ***$P < 0.001$.

labeling conditions were tested to achieve a balance between labeling efficiency and cGAS activity. Optimized labeling conditions achieved close to 100% labeling efficiency for cGAS while preserving its enzymatic activity and phase separation ability, indicating minimal perturbation during the labeling process (Fig. S1A-C). As previous reported, 10 μM labeled cGAS can form micron-scale condensates with 10 μM 99 bp double-stranded DNA (dsDNA) (Fig. S1D). Fluorescence recovery after photobleaching (FRAP) experiments confirmed that these condensates

were liquid-like and retained fluidity (Fig. S1E). With our optimized labeling procedures, the activity of labeled cGAS was almost the same as the unlabeled one (Fig. S1F). As expected, human G3BP1 and PCBP1 proteins moderately enhanced cGAS-dsDNA phase separation and the enzymatic activity of cGAS, whereas viral tegument proteins ORF9, ORF52 and VP22 inhibited cGAS phase separation and reduced its enzymatic activity (Fig. 1A-C, Fig. S1G, S2). Labeling had little or no effect on the regulatory effects of these proteins.

With dcFCCS method (Fig. 1D), we quantified hydrodynamic radii of the condensates formed by AF488 labeled cGAS (AF488-cGAS) and 99 bp Cy5 labeled dsDNA (Cy5-dsDNA) at the nanomolar range in the presence of human or viral proteins. BSA was used as the control sample. Overall, high cGAS and dsDNA concentrations led to the formation of large cGAS-dsDNA heterocomplexes or condensates (Fig. 1E-H, Fig. S1H). G3BP1 and PCBP1 moderately enhanced the size of cGAS-dsDNA condensates at high concentrations (Fig. 1F, [cGAS] ≥2 nM) and increased proportions of cGAS and dsDNA within the heterocomplexes at low concentrations (Fig. 1G, H, [cGAS] 0.5 nM and 1 nM). In the presence of ORF9, ORF52, or VP22 proteins, the size of the condensate was greatly reduced (Fig. 1F) and the critical concentrations to have most of cGAS and dsDNA molecules participating in condensate formation increased ~5 folds (from 2 nM to 10 nM, Fig. 1G-H). The stoichiometry of AF488-cGAS and 99 bp Cy5-dsDNA in the condensates was ~ 0.5, which was barely affected by G3BP1 or PCBP1 and was reduced to ~ 0.3 by ORF9, ORF52 or VP22 (Fig. 1I, Fig. S1I-L). We further quantified the interaction of the cGAS activity-promoting proteins G3BP1 and PCBP1 with cGAS. The proportions of G3BP1 and PCBP1 within heterocomplexes or condensates were higher at low concentrations (Fig. 1J-K, [cGAS] < 10 nM), but decreased by 1–2 orders of magnitude at high concentrations ([cGAS] ≥10 nM). The size of particles containing G3BP1 and PCBP1 decreased significantly at high concentrations (Fig. 1L-M), while the size of condensates containing cGAS increased progressively with the increase of concentration (Fig. 1L-M). Together, these phenomena further confirmed the ability of G3BP1, PCBP1, ORF9, ORF52, and VP22 in regulating LLPS of cGAS and dsDNA.

Condensate formation is regulated by binding affinities of accessory proteins with cGAS and dsDNA

To our knowledge, none of the accessory proteins we tested directly interact with the catalytic center of cGAS. These proteins all regulate the LLPS of cGAS to affect its activity. Since the interactions between molecules are the fundamental driving forces of LLPS[27], we speculate that the difference of these proteins in affecting LLPS is caused by their different binding affinities with cGAS and dsDNA.

DcFCCS can quantify the binding affinity (K_d) between two molecules labeled with different fluorophores. We first labeled G3BP1, PCBP1, ORF9, ORF52, and VP22 with AF488 (Table S1) and verified their functions in promoting or inhibiting cGAS activity after labeling (Fig. S2). 25 bp short dsDNA was used, instead of 99 bp dsDNA, to prevent LLPS and to provide accurate quantification of binding affinities between proteins and dsDNA[25]. K_d between AF488-cGAS and 25 bp Cy5-dsDNA was 160 ± 30 nM (Fig. 2A, B), consistent with our reported value[25]. K_d for G3BP1 or PCBP1 to bind to 25 bp dsDNA was ~400 nM, whereas binding affinities between viral tegument proteins (ORF9, ORF52, and VP22) and 25 bp dsDNA were stronger (K_d ~ 100 nM, Fig. 2C-D and Fig. S3A-C). Binding affinities between cGAS and accessory proteins also displayed significant differences. Binding affinities between cGAS and viral tegument proteins were weak with K_d ~ 2000 nM, whereas binding affinities between cGAS and G3BP1 or PCBP1 were ~12 folds stronger, respectively (Fig. 2E, F and Fig. S3D, E).

Thus, the abilities of these accessory proteins to enhance or to inhibit phase separation and activity of cGAS is likely dominated by their binding affinities with cGAS and dsDNA (Fig. 2G). Proteins, such as G3BP1 or PCBP1, which interact with both cGAS and dsDNA, would facilitate cGAS-DNA LLPS and promote cGAS activity[16,18]. On the other hand, viral tegument proteins, which strongly interact with dsDNA but bind to cGAS weakly, compete with cGAS for binding to dsDNA and could even exclude cGAS from the condensed phase to inhibit cGAS activity[19,21]. If our proposed mechanism is correct, chemical- and light-inducible cGAS immune signaling modulators can be engineered by modulating the strength of intermolecular interactions between accessory proteins and cGAS.

Chemical-inducible cGAS phase separation and activities in tubes

Based on the quantitative analysis shown in Fig. 2G, we proposed that regulating the interactions among cGAS, dsDNA and accessory proteins would affect cGAS phase separation and activity.

Rapamycin-induced heterodimerization of FKBP and FRB proteins is a commonly used method to modulate interactions between two molecules of interests[28–30]. To generate a rapamycin-inducible cGAS phase separation, we fused the FRB to the C-terminus of cGAS and the FKBP to the N-terminus of viral tegument proteins (Table S3). Fusion of FRB or FKBP had almost no influence on their interactions with dsDNA (Fig. S4A) and the binding affinities between cGAS and viral tegument proteins (Fig. S4B). Consistent with our design, the presence of rapamycin strengthened the interactions between cGAS-FRB and FKBP-viral tegument proteins by two orders of magnitude, whereas rapamycin had almost no influence on interactions between cGAS and viral tegument proteins in the absence of FKBP and FRB (Fig. 3A-C). Next, we examined rapamycin-induced cGAS phase separation and activation in test tubes. We have shown that viral tegument proteins could exclude cGAS from the condensed phase to inhibit cGAS activity (Fig. S4C). Rapamycin induced cGAS-FRB to re-enter the condensed phase within 2 min (Fig. 3D), whereas cGAS without FRB cannot re-enter (Fig. S4D). In addition, rapamycin boosted cGAS-FRB activity in the presence of FKBP-viral tegument proteins by 2–5 folds (Fig. 3E).

As shown in Fig. 2G, viral tegument proteins exhibit stronger DNA binding affinities than G3BP1 or PCBP1. We generated three ORF9 variants, by mutating K180A/R181A, R188A/R189A, and K180A/R181A/R188A/R189A, respectively. All of them exhibited attenuated binding affinities with DNA (Fig. 3F)[20]. The inhibitory effects of ORF9 variants on cGAS enzyme activity were all attenuated as well (Fig. 3G, left). Similarly, rapamycin boosted cGAS-FRB activity in the presence of FKBP-ORF9 variants by 1–3 folds (Fig. 3G, right), whose enhancement is less effective than the WT-ORF9 (Fig. 3E).

Further validation was performed on the cGAS activity-promoting proteins G3BP1 and PCBP1. Based on Predictions of AlphaFold4 and previous studies[16,17], a series of protein mutants and truncations were constructed, which had weakened binding to cGAS (Fig. 3H). Consistent with our proposed mechanism based on the results of viral tegument proteins, these G3BP1 variants and PCBP1 variants with diminished cGAS binding could even inhibit cGAS activity (Fig. 3I, J). When the FKBP domain was fused to the N-terminus of G3BP1 and PCBP1 and rapamycin was present to strengthen the interactions between cGAS-FRB and FKBP-G3BP1 or FKBP-PCBP1 (Fig. 3K), the activity of cGAS was only moderately promoted (Fig. 3L). Together, these results confirmed our hypothesis that regulating the interactions among the cGAS, dsDNA, and accessory proteins can affect cGAS phase separation and activity controllable regulation. A delicate balance is needed to promote cGAS activity with high efficiency.

Chemical-inducible cGAS phase separation and signaling in living cells

Based on our assays in test tubes (Fig. 3), strengthening the interactions between viral tegument proteins and cGAS would transform their effects on cGAS activation from repressing to promoting with the highest enhancement ratio, providing molecular basis to engineer chemical- and light-inducible cGAS immune signaling systems.

Subsequently, we examined chemical-inducible cGAS phase separation and signaling in HEK293T cells to enhance the applicability of our regulation system. N-terminus of cGAS variants was further fused with mCherry, whereas N-terminus of viral tegument proteins was further fused with EGFP. In the absence of rapamycin, puncta of viral tegument proteins exhibited low colocalization with mCherry-cGAS (Fig. S4E). Addition of rapamycin induced cGAS-FRB to rapidly enter puncta of viral tegument proteins within 5–15 min (Fig. 4A-I, Fig. S4F), whereas cGAS without FRB was not affected by rapamycin (Fig. S4G-K). The downstream immune
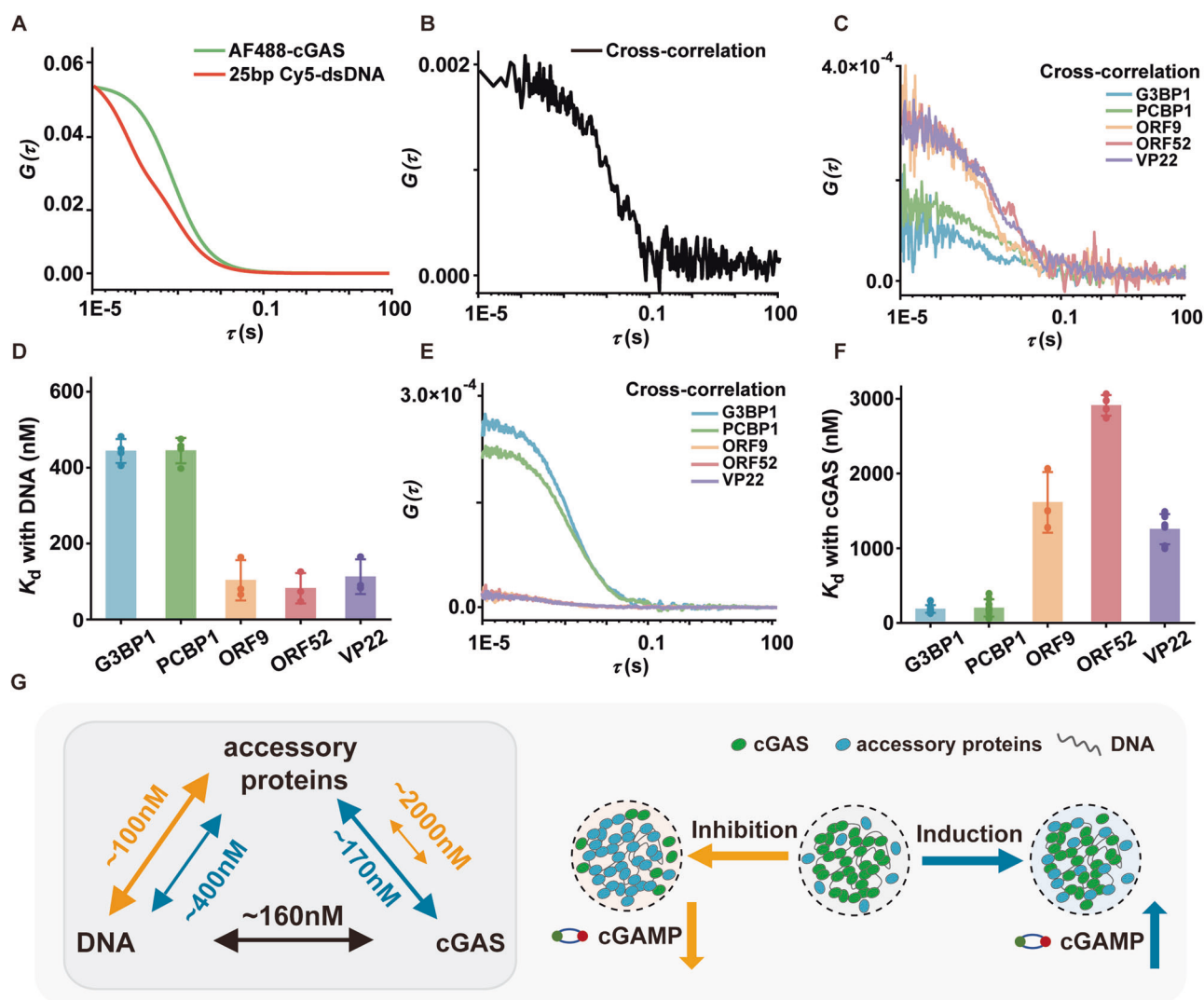
Fig. 2 | Binding affinities among cGAS, dsDNA, and accessory proteins quantified by dcFCCS. A Autocorrelation curves of 10 nM AF488-cGAS (green) and 20 nM Cy5-dsDNA (red). **B** The cross-correlation curve between AF488-cGAS and Cy5-dsDNA calculated from the same measurement as shown in (**A**). **C** Cross-correlation curves of 10 nM AF488-accessory proteins and 20 nM Cy5-dsDNA. **D** Binding affinities between AF488-accessory proteins and 25 bp Cy5-dsDNA.

E Cross-correlation curves of 10 nM AF488-proteins and 20 nM Cy5-cGAS. **F** Binding affinities between AF488-proteins and Cy5-cGAS. **G** Binding affinities among accessory proteins, cGAS, and dsDNA. Values of proteins promoting cGAS activity are shown in blue, whereas values of proteins repressing cGAS activity are shown in yellow. Data are presented as mean ± SEM (N = 3), with individual points plotted in bar graphs.

signaling of cGAS exhibited similar behaviors. The phosphorylation levels of TBK1 and IRF3 in the cells, which were inhibited by the viral tegument proteins, can be enhanced by rapamycin (Fig. 4J-L, Fig. S5A-C) when using FKBP and FRB fused proteins. In the absence of FKBP and FRB, rapamycin had almost no influence (Fig. S5). Expression level of *IFN-β* mRNA, another indicator of cGAS downstream signaling, was inhibited by the viral tegument proteins and can also be enhanced by rapamycin (Fig. S6). Together, these results confirmed that our engineered system enables chemical-inducible cGAS phase separation and immune signaling both in test tubes and in living cells.

Light-inducible cGAS phase separation and signaling
Light-inducible approaches usually exhibit higher spatial and temporal precision than chemical-inducible ones. Thus, we used the light-inducible modulator pMag-nMagHigh1[28,31], to generate a light-inducible cGAS phase separation and signaling system. We fused the pMag to the C-terminus of cGAS and the nMagHigh1 to the N-terminus of viral tegument proteins (Table S3). We used dcFCCS to quantify the extent of heterodimer formation, when a mixture of cGAS-pMag and nMagHigh1-viral tegument

proteins was exposed to blue light (Fig. 5A–C). In accordance with our design, the proportions of cGAS-pMag and nMagHigh1-viral tegument proteins forming heterodimer increased by ~5 folds to 60–90% under blue light, whereas interactions between cGAS and viral tegument proteins were barely affected by blue light irradiation in the absence of pMag and nMagHigh1 (Fig. S7A, B).

Next, we also examined light-induced cGAS phase separation and activation in test tubes. After viral tegument proteins excluded cGAS from the condensed phase (Fig. S4C), blue light-induced cGAS-pMag re-enter the condensed phase within 5 min (Fig. 5D), whereas cGAS without pMag cannot re-enter (Fig. S7C). In addition, cGAS-pMag activity was boosted by 2–5 folds after 120-min blue light irradiation (Fig. 5E).

We subsequently examined light-inducible cGAS phase separation and signaling in HEK293T cells. Fluorescent tags were added as previously described in the chemical-inducible system. Without the irradiation of blue light, puncta of viral tegument proteins exhibited low colocalization with mCherry-cGAS (Fig. S7D). Irradiation of blue light-induced cGAS-pMag to rapidly enter puncta of viral tegument proteins within 5–10 min (Fig. 5F-K, Fig. S7E), whereas cGAS without pMag was not affected by blue light
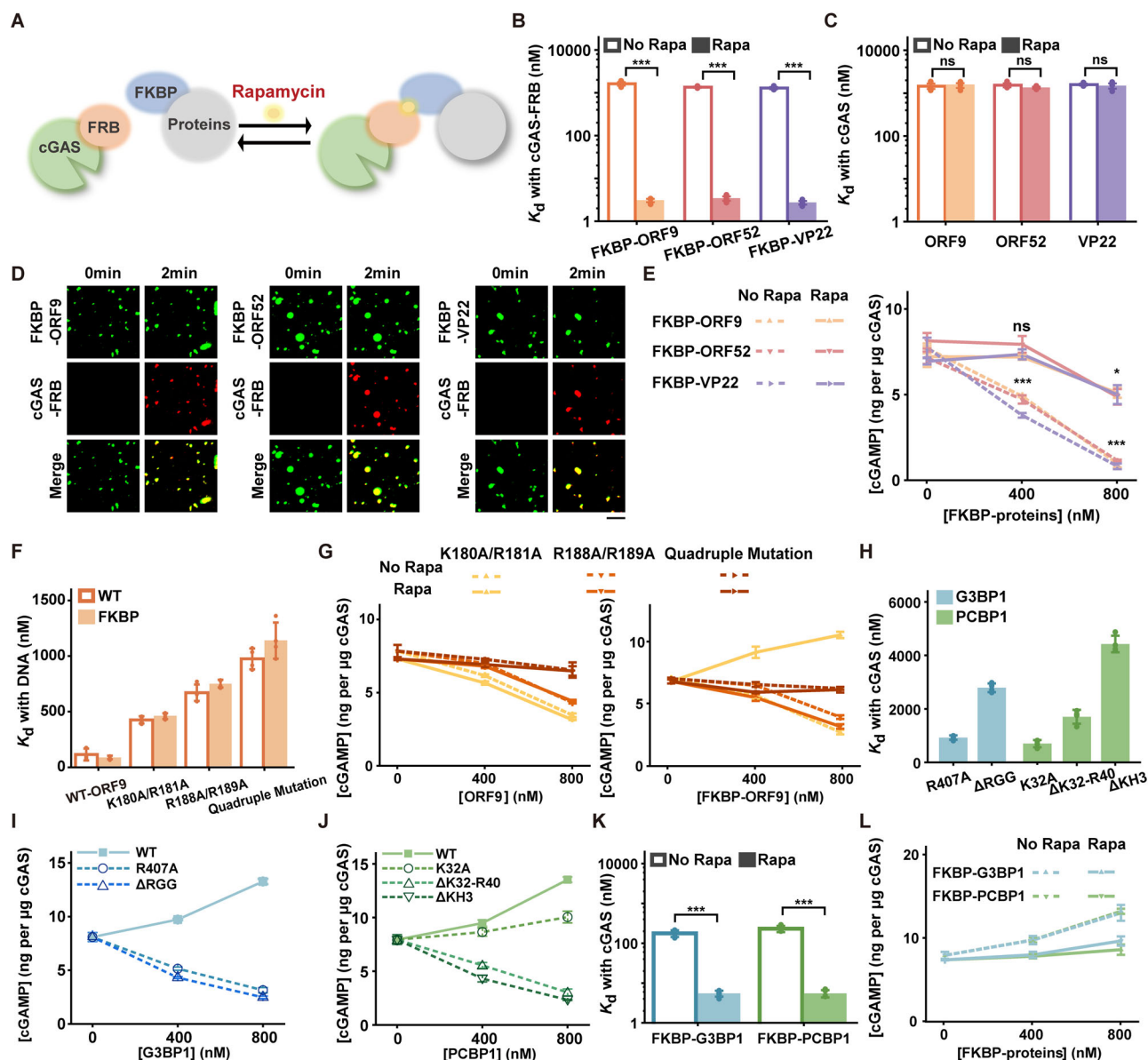
Fig. 3 | Chemical-inducible cGAS phase separation in tubes. A Rapamycin-induced heterodimerization of cGAS-FRB and FKBP-proteins. **B** Binding affinities between AF488-FKBP-proteins and Cy5-cGAS-FRB with or without 200 nM rapamycin. **C** Binding affinities between AF488-proteins and Cy5-cGAS with or without 200 nM rapamycin. **D** 200 nM rapamycin induced phase separation of 5 μM AF488-FKBP-proteins, 5 μM Cy5-cGAS-FRB, and 5 μM 99 bp dsDNA. Scale bar: 5 μm. **E** The cGAMP production of 0, 400, or 800 nM cGAS-FRB mixed with 100 nM dsDNA in the presence of 100 nM viral tegument FKBP-proteins with or without 200 nM rapamycin. **F** Binding affinities between AF488-ORF9 mutation proteins and 25 bp Cy5-dsDNA. **G** The cGAMP production of 100 nM cGAS mixed with 100 nM dsDNA in the presence of 0, 400, or 800 nM ORF9 proteins with or without 200 nM rapamycin. Proteins without FKBP tag(left). Proteins with FKBP tag(right). **H** Binding affinities between G3BP1 and PCBP1 mutation proteins and cGAS. **I** The

cGAMP production of 100 nM cGAS mixed with 100 nM dsDNA in the presence of 0, 400, or 800 nM G3BP1 wildtype and mutation proteins. **J** The cGAMP production of 100 nM cGAS mixed with 100 nM dsDNA in the presence of 0, 400, or 800 nM PCBP1 wildtype and mutation proteins. **K** Binding affinities between AF488-FKBP-G3BP1 or AF488-FKBP-PCBP1 and Cy5-cGAS-FRB with or without 200 nM rapamycin. **L** The cGAMP production of 100 nM cGAS-FRB mixed with 100 nM dsDNA in the presence of 0, 400, or 800 nM FKBP-proteins with or without 200 nM rapamycin. Data are presented as mean ± SEM (N = 3). The time points of (**D**) were initiated from the inclusion of rapamycin. Statistical significance was assessed by two-tailed unpaired t test in (**B**, **C**, **E**, and **K**). Statistical differences in (**E**) were made relative to the controls without the addition of protein. Statistical differences were represented as follows: ns not significant, *$P < 0.05$, ***$P < 0.001$.

(Fig. S7F-J). cGAS-pMag was removed from puncta of viral tegument proteins 5 h after blue light irradiation was switched off, indicating light-inducible cGAS phase separation is reversible (Fig. 5L-N and Movie S1). In addition, light-inducible cGAS phase separation can be confined within a single cell within the field of interest, confirming its high spatial precision (Movie S 2). The downstream immune signaling of cGAS exhibited similar behaviors after light-inducible activation. The phosphorylation levels of TBK1 and IRF3 in the cells, which were inhibited by the viral tegument proteins, can be enhanced by constant blue light irradiation (Fig. 5O-Q,

Fig. S8A-C) when using pMag and nMagHigh1 fused proteins. In the absence of pMag and nMagHigh1, irradiation had almost no influence (Fig. S8). Together, these results validated our engineered light-inducible cGAS phase separation and signaling system both in test tubes and in living cells.

Discussion

Previous studies have shown that several human and viral proteins are capable to enhance or inhibit the enzymatic activity of cGAS by affecting its
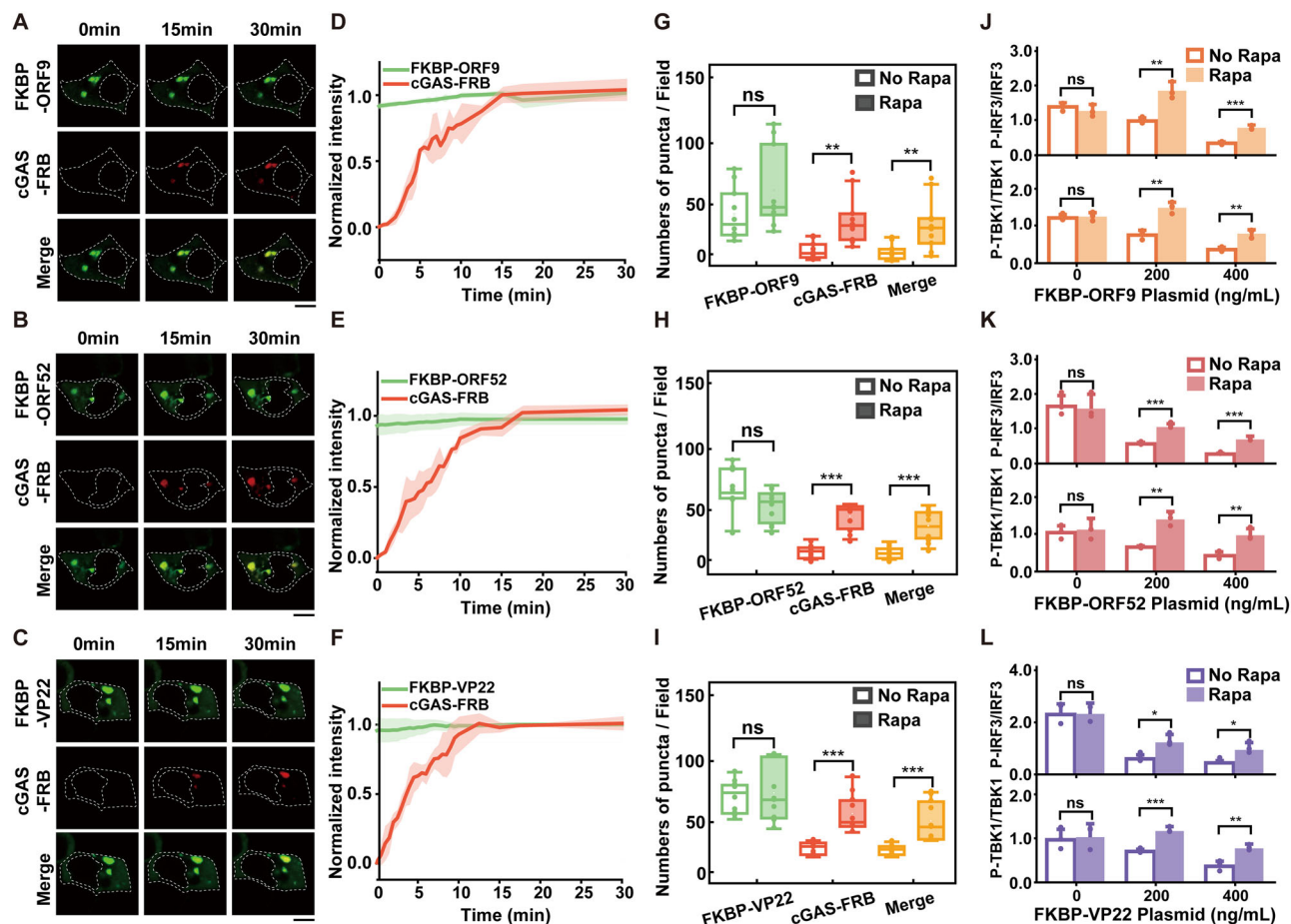
Fig. 4 | Chemical-inducible cGAS phase separation and signaling in cells.
A–C Rapamycin induced phase separation of EGFP-FKBP-proteins and mCherry-cGAS-FRB in HEK293T cells. Scale bar: 10 μm. **D–F** Plots of normalized fluorescence intensity of FKBP-proteins and cGAS-FRB over 30 min time course after adding rapamycin. Data are collected from 3 cells. **G–I** Counts of intracellular puncta with or without rapamycin. Box plots depict the first quartile and third quartile with median as center and min-max values for whiskers, hollow squares represent average

values, except for outliers calculated as data points ±1.5× interquartile range. (N = 10) **J–L** Bar graphs showed the relative abundance of phosphorylated IRF3 and TBK1 to total IRF3 and TBK1 proteins analyzed by Western blotting shown in Fig. S5A–C. (N = 3) The time points of (**A–C**) were initiated from the inclusion of rapamycin. Data are presented as mean ± SEM. Statistical significance was assessed by two-tailed unpaired t test in (**G-L**). Statistical differences were represented as follows: ns not significant, *P < 0.05, **P < 0.01, ***P < 0.001.

phase separation with dsDNA[15]. The molecular basis leading to LLPS of biomolecules are multivalent interactions between molecules[12,32]. To reveal the molecular mechanisms of these accessory proteins exerting the enhancement or inhibition effects, we applied the dcFCCS technique to systematically examine the phase separation of cGAS, dsDNA, and accessory proteins and the binding affinities among these components[24]. Our works revealed that the binding strength between the proteins and cGAS determined whether their effects are repressing or promoting.

The cGAS activity-promoting proteins G3BP1 and PCBP1 exhibit relatively strong binding affinities with cGAS (Fig. 2G). They are capable of pre-binding to cGAS to form primary condensates, which can effectively promote the binding and phase separation of cGAS and dsDNA to enhance cGAS enzymatic activity[16–18]. Similar mechanism has been discovered when RNA activates cGAS through forming primary condensates with cGAS, thereby enabling dsDNA at low concentration to enter the cGAS-RNA droplets and to activate immune signaling[33]. In contrast, viral tegument proteins, which have been shown to inhibit the phase separation and enzymatic activity of cGAS[19–23], exhibit weak interactions with cGAS, accompanied by stronger binding with dsDNA than with cGAS. Thus, cGAS is excluded from liquid condensates and replaced by viral tegument proteins, which leads to reduction of cGAS activity. Attenuating binding between viral tegument protein ORF9 and dsDNA can only diminish its inhibitory effects on cGAS, but could not promote cGAS activity. Thus, the binding strength between accessory proteins and cGAS seems to be the key

factor and provides a rational explanation at the molecular level regarding how these proteins regulate LLPS and activity of cGAS.

LLPS of biomolecules has been shown to play essential roles in many important cellular processes[34]. Thus, chemical-inducible and light-inducible LLPS systems have been engineered and served as powerful tools for regulating processes such as transcription[35], protein endocytosis and polymerization[36], and vesicles delivery[37]. The molecular basis of these tools was either chemical-induced multivalent interactions[37–39] or light-induced multivalency via Cry2 oligomerization[35,36,40,41]. In this study, inspired by the molecular mechanisms of human and viral proteins to enhance or inhibit the LLPS and activity of cGAS, we proposed to modulate binding strength between viral proteins and cGAS via a single interaction site through a chemical-inducible FRB-FKBP dimerization system[28,30] and a light-inducible pMag-nMagHigh1 dimerization system[28,31], which enable us to successfully develop a chemical-inducible strategy and a light-inducible strategy, respectively, to manipulate cGAS phase separation and immune signaling in test tubes and in living cells. The light-inducible approach exhibited excel spatial and temporal precise to regulate phase separation and signaling in a reversible manner, which can be further fined tuned with different variants of pMag-nMagHigh1 dimerization system exhibiting distinctive switch-on and switch-off kinetics[28,31]. Our phase separation regulatory system is applicable to other accessory proteins that utilize similar mechanisms to regulate cGAS phase separation and activity, such as cGAS activity-promoting proteins ZCCHZ3[42] and PQBP1[43], as well as inhibitory
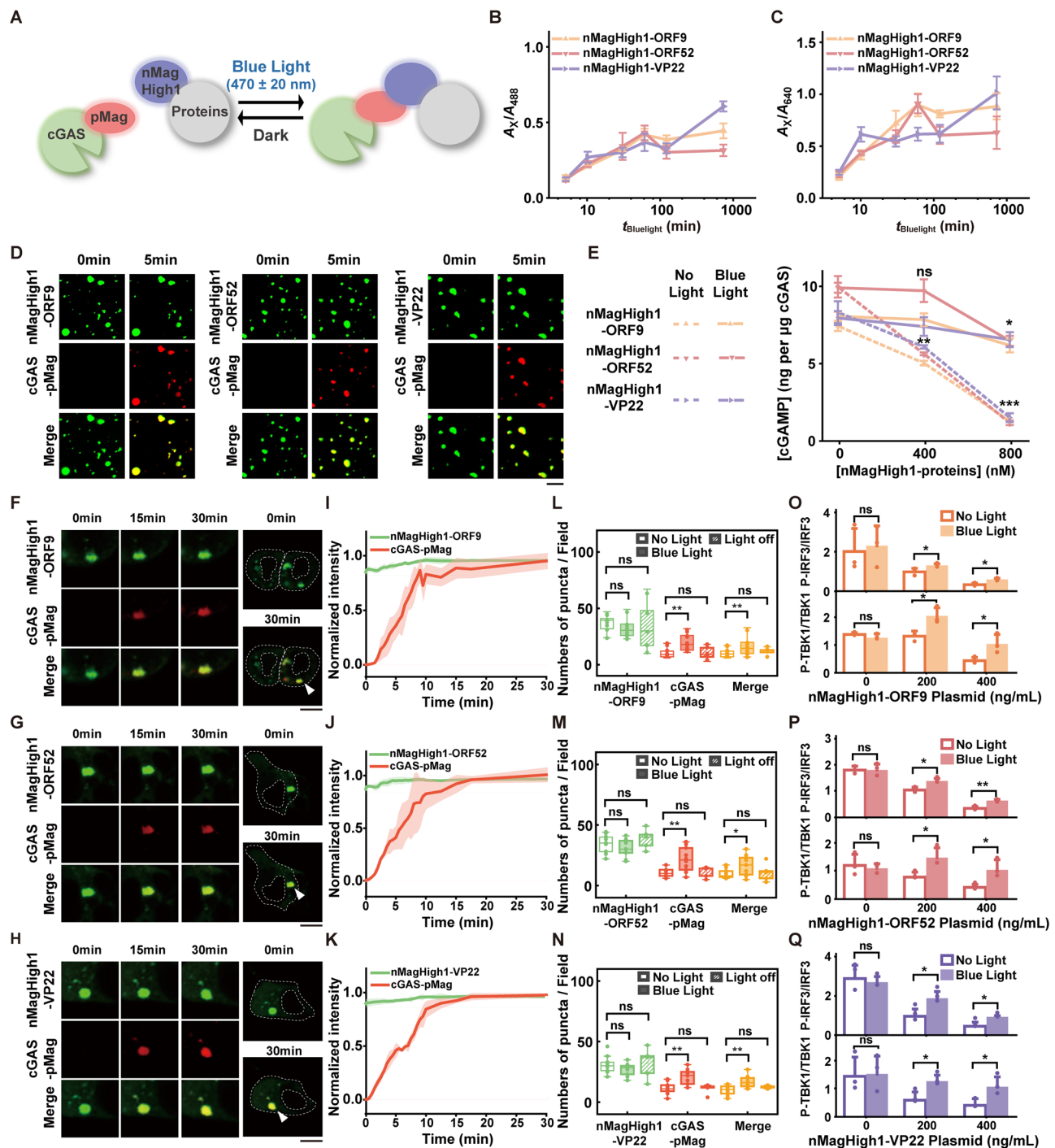
Fig. 5 | Light-inducible cGAS phase separation and signaling. A Light-induced heterodimerization of cGAS-pMag and nMagHigh1-proteins. **B** A_X/A_{488} estimating proportions of Cy5-cGAS-pMag participating in heterocomplexes, which increased over 2-h blue light illumination (N = 3). **C** A_X/A_{640} estimating proportions of AF488-nMagHigh1-proteins participating in heterocomplexes, which increased over 2-h blue light illumination. 10 nM Cy5-cGAS-pMag and 20 nM AF488-nMagHigh1-proteins were used. (N = 3) **D** Blue light-induced phase separation of 5 μM AF488-nMagHigh1-proteins, 5 μM Cy5-cGAS-pMag, and 5 μM 99 bp dsDNA. Scale bar: 5 μm. **E** cGAMP production of 100 nM cGAS-pMag mixed with 100 nM dsDNA in the presence of 0, 400, or 800 nM viral tegument proteins with or without 2-h blue light irradiation. (N = 3) **F–H** Blue light irradiation induced phase separation of EGFP-nMagHigh1-proteins and mCherry-cGAS-pMag in HEK293T cells. Scale bar: 10 μm. **I–K** Plots of the normalized fluorescence intensity of

nMagHigh1-proteins and cGAS-pMag over 30 min time course after irradiation. Data are collected from 3 cells. **L–N** Counts of intracellular puncta with or without blue light irradiation and 5 h after light switched off. Box plots depict the first quartile and third quartile with median as center and min-max values for whiskers, hollow squares represent average values, except for outliers calculated as data points ±1.5 × interquartile range (N = 10). **O–Q** Bar graphs showed the relative abundance of phosphorylated IRF3 and TBK1 to total IRF3 and TBK1 proteins analyzed by Western blotting shown in Fig. S8A–C. (N = 3) The time points of (**D**, **F–H**) were initiated from the blue light irradiation. Data are presented as mean ± SEM. Statistical differences in E were made relative to the controls without the addition of nMaghigh1-protein and assessed by two-tailed unpaired t test in (**E**) and (**L-Q**). Statistical differences were represented as follows: ns not significant, *P < 0.05, **P < 0.01, ***P < 0.001.

Article

proteins HCMV UL31[44] and UL42[45]. In addition, our approach can be extended to multi-component LLPS systems and other cGAS-dsDNA-accessory protein-like systems, including NPR1-CRL3-dsDNA[46], Lge1-Bre1-Nucleosomes[47], etc. Thus, our mechanistic insights offer guidance and new avenues to manipulate multi-component, especially protein-nucleic acid, phase separation systems in cells with high temporal and spatial specificity.

Materials and methods

Plasmids construction
The full-length cGAS (amino acids 1-522) was cloned into the pET-28a vector with a SUMO tag at the N-terminus. The FRB tag (with an EFGGSGSSGGSGGSGGSG linker) or the pMag tag (with an EFGGSGSSGGSG linker) was fused at the C-terminus of cGAS. The mCherry was further fused at the N-terminus of cGAS to form mCherry-cGAS, mCherry-cGAS-FRB, and mCherry-cGAS-pMag, respectively.

The coding sequences of G3BP1 and PCBP1 were cloned from a human cDNA library which was a gift from Dr. Jizhou Li (Tsinghua University), and subsequently inserted into the pET-28a vector with a SUMO tag at the N-terminus.

The viral tegument proteins KSHV-ORF52, HSV1-VP22 and VZV-ORF9 sequences were synthesized by Sangon Biotech and subsequently cloned into the pET-28a vector with a SUMO tag at the N-terminus. The FKBP tag (with a GGSGGSGGGSGSGSGGGT linker) or the nMagHigh1 tag (with a GGSGGSGGGSGSGSGGGT linker) was fused at the N-terminus of viral tegument proteins. The EGFP was further fused at the N-terminus of viral tegument proteins to form EGFP-viral tegument proteins, EGFP-FKBP-viral tegument proteins, and EGFP-nMagHigh1-viral tegument proteins, sequentially.

Proteins expression and purification
cGAS proteins were expressed in $2 \times$ Yeast Extract and Tryptone ($2\times$YT) medium via *Escherichia coli* (*E. coli*) strain Rosetta (DE3) and induced with 200 μM isopropyl β-D-thiogalactoside (IPTG) at 18 °C for 19 h. The cells expressing proteins were collected and lysed by sonication (2 s of sonication at 4 s intervals) in the lysis buffer (20 mM HEPES pH 7.5, 400 mM NaCl, 30 mM imidazole, 10% glycerol, 1 mM Tris (2-carboxyethyl) phosphine (TCEP), and 1 mM PMSF) for 40 min. Subsequently, the clarified supernatant was incubated with Ni-NTA beads (GE Healthcare) for 2 h at 4 °C, then the proteins were eluted with 20 mM HEPES pH 7.5, 400 mM NaCl, 300 mM imidazole, 10% glycerol, 1 mM TCEP. Subsequently, the His$_6$ SUMO tag was removed by the SUMO protease (Ulp1) with a Ulp1: protein ratio 1:20 (w/w) at 4 °C overnight. The cleaved proteins were purified by a HiTrap™ Heparin HP column (GE Healthcare) and eluted with a gradient from 0.25 M to 1.5 M NaCl in 20 mM HEPES pH 7.5, 10% glycerol, 1 mM TCEP. The eluted proteins were concentrated and purified by size exclusion chromatography on a Superdex™ 200 Increase 10/300 GL column (GE Healthcare) in 20 mM HEPES pH 7.5, 150 mM KCl, 10% glycerol, 1 mM TCEP. The proteins were flash frozen by liquid nitrogen and stored at −80 °C. cGAS-FRB and cGAS-pMag were purified via the same procedure.

G3BP1 and PCBP1 proteins were expressed in Luria-Bertani (LB) medium via *E. coli* strain BL21 (DE3) and induced with 500 μM IPTG at 16 °C for 16 h. The cells were collected and lysed in a solution of 50 mM HEPES 7.5 in 250 mM NaCl, 20 mM imidazole, 1 mM TCEP, 5% glycerol, sonicated (2 s of sonication at 4 s intervals) for 30 min. Subsequently, the supernatant was loaded onto Ni-NTA bead (GE Healthcare) and the proteins were eluted with elution buffer (50 mM HEPES 7.5, 250 mM NaCl, 500 mM imidazole, 1 mM TCEP, 5% glycerol). The His$_6$ SUMO tags were cleaved by Ulp1 at 4 °C overnight. The cleaved protein samples were subjected to a HiTrap™ Heparin column (GE Healthcare) with a linear NaCl gradient from 300 mM to 1 M in a solution of 50 mM HEPES 7.5, 10% glycerol, 1 mM TCEP. The eluted proteins were subjected to size exclusion chromatography on a Superdex™ 200 Increase 10/300 GL column (GE Healthcare) in 20 mM HEPES 7.5, 300 mM NaCl, 1 mM TCEP. The peak samples were concentrated, flash-frozen by liquid nitrogen and stored at −80 °C.

The viral tegument proteins were expressed in LB medium via *E. coli* strain Rosetta (DE3) and induced with 500 μM IPTG at 18 °C overnight. The cells expressing His$_6$ SUMO-tagged proteins were collected. Protease Inhibitor Cocktail Tablets (Roche) were added before lysis to inhibit the general degradation of proteins. The cells were harvested and lysed by sonication (2 s of sonication at 4 s intervals) for 30 min in 50 mM Tris-HCl pH 7.5, 500 mM NaCl, 20 mM imidazole, 1 mM TCEP, 5% glycerol. Subsequently, the supernatant was loaded onto Ni-NTA bead (GE Healthcare), and proteins were eluted with the elution buffer (50 mM Tris-HCl pH 7.5, 500 mM NaCl, 500 mM imidazole, 1 mM TCEP, 5% glycerol). His$_6$ SUMO tags were cleaved by Ulp1 at 4 °C overnight. The cleaved protein samples were subjected to a HiTrap™ heparin column (GE Healthcare) with a linear NaCl gradient from 300 mM to 1 M to remove the His$_6$ SUMO tag and nucleic acids. The eluted protein KSHV-ORF52 was subjected to size exclusion chromatography on a Superdex™ 200 Increase 10/300 GL column (GE Healthcare) in 20 mM HEPES 7.5, 300 mM NaCl, 1 mM TCEP. And the proteins HSV1-VP22 and VZV-ORF9 were eluted from Superdex™ 200 Increase 10/300 GL column in buffers containing 600 mM and 500 mM NaCl, respectively. The peak samples were concentrated, measured, and flash frozen by liquid nitrogen and long-term stored at −80 °C. The FKBP-viral tegument proteins and nMagHigh1-viral tegument proteins were purified via the same procedure.

Protein labeling
cGAS proteins were mixed Alexa Fluor™ 488 (AF488) NHS ester (ThermoFisher Scientific) or Cyanine5 (Cy5) NHS ester (Lumiprobe) in a 1:2 (protein:dye) molar ratio in the buffer (20 mM HEPES pH 7.5, 150 mM KCl, 10% glycerol, 1 mM TCEP) and incubated at 23 °C for 20 min. G3BP1 and PCBP1 were mixed with AF488 in the buffer (20 mM HEPES pH 7.5, 300 mM NaCl, 10% glycerol, 1 mM TCEP) in a molar concentration ratio of 1:3 and incubated at 23°C for 2 h. Viral tegument proteins were labeled with AF488 in the buffer (20 mM HEPES pH 7.5, 300 mM NaCl, 10% glycerol, 1 mM TCEP) at a molar concentration ratio of 1:5 and incubated at 4°C overnight. The labeled proteins were separated from the excess free dyes by Superdex™ 200 Increase 10/300 GL column (GE Healthcare). Based on absorbance of different components and the molar extinction coefficients, we quantified the concentrations of the different components using A_{280} (protein), A_{495} (dye AF488) and A_{652} (dye Cy5). Labeling efficiency was determined by the ratio of fluorophore concentration to protein concentration (Tables S1 and S2).

dsDNA labeling
Single-stranded DNAs of 25 bp and 99 bp were synthesized by Sangon Biotech. DsDNA molecules were formed by annealing forward and reverse ssDNA in the buffer (20 mM Tris-HCl pH 7.5, 50 mM NaCl). All DNA sequences are listed in Table S4.

Synthesized DNA oligonucleotides with NH$_2$ modified at the 5' end (Sangon Biotech) were mixed with Cyanine5 NHS ester (Lumiprobe) at a 1:10 molar ratio and incubated overnight at room temperature. Labeled DNA was isolated from excess free dyes by ethanol precipitation. Dye labeling efficiencies were calculated based on the molar extinction coefficients of DNA at 260 nm and Cy5 at 652 nm, respectively. All DNA oligonucleotides were ~100% labeled.

In vitro phase separation of cGAS and dsDNA
Proteins were incubated with dsDNA in 96-well plates (Corning) pre-coated with 20 mg/mL BSA (Sigma) to a final volume of 50 μL. Phase separation of cGAS with dsDNA was performed by gently mixing 10 μM 99 bp dsDNA (containing 200 nM Cy5 labeled dsDNA) and 10 μM cGAS (containing 200 nM AF488 labeled cGAS) in 5 mM Tris-HCl pH 7.5, 300 mM NaCl, 1 mM DTT, 1 mg/mL BSA. The time-lapse experiments were conducted on an FV1200 (Olympus) confocal microscope using the 60×/1.42 NA oil objective. Images were captured every 30 s over 20 min. The time-lapse images were processed with ImageJ.

In vitro phase separation of cGAS and dsDNA affected by accessory proteins

In general, Cy5-cGAS and dsDNA were first incubated for 10 min to form phase separation in 96-well plates (Corning) pre-coated with 20 mg/mL BSA (Sigma) to a final volume of 45 μL in 5 mM Tris-HCl pH 7.5, 300 mM NaCl, 1 mM DTT, 1 mg/mL BSA, followed by the addition of 5 μL AF488-accessory proteins. The experiments were conducted on an FV1200 (Olympus) confocal microscope using the 60×/1.42 NA oil objective. Images were captured every 30 s over 20 min. The time-lapse images were processed with ImageJ.

In vitro FRAP assay

Fluorescence recovery after photobleaching (FRAP) assays were performed on an FV1200 (Olympus) confocal microscope at room temperature. For FRAP, 10 μM AF488-cGAS and 10 μM 99 bp Cy5-dsDNA were pre-incubated for 30 min in 5 mM Tris-HCl pH 7.5, 150 mM NaCl, 1 mM DTT, 1 mg/mL BSA, spots of 2 μm diameter in 10 μm droplets were photobleached using a 488 nm laser. The recovery images were acquired with 15 s intervals in 15 min after bleaching. Fluorescence intensities of the interest regions (ROI) were normalized to 1 before bleaching. Image intensities were measured by Mean ROI, which can be obtained with the intensity of the interested regions subtracting the real-time intensity of the background.

Analysis of dcFCCS data

Raw data on photon arrival times and FCCS curves were recorded within 5 min of mixing the samples. For each case, the dcFCCS measurements were repeated at least three times. Autocorrelation curves of AF488 and Cy5 detection channels were fitted by Eq. 1[25].

$$G(\tau) = A \frac{1}{\left(1 + \frac{\tau}{\tau_D}\right)} \frac{1}{\sqrt{1 + \frac{\tau}{a^2 \tau_D}}} \left(1 + \frac{T}{1 - T} \times e^{-\frac{\tau}{\tau_{tri}}}\right) \quad (1)$$

in which A is the amplitude of the autocorrelation curve, τ_D is the diffusion time of the labeled molecules, T is the triplet-state fraction, τ_{tri} is the relaxation time of the triplet state, and a is the ratio of the vertical radius of the laser over its horizontal radius. Herein, A_{488} and A_{640} were calculated as the amplitudes of the autocorrelation curves of AF488 and Cy5 detection channels, respectively. The cross-correlation curves were fitted using Eq. 2[25].

$$G_X(\tau) = A_X \frac{1}{\left(1 + \frac{\tau}{\tau_{Dx}}\right)} \frac{1}{\sqrt{1 + \frac{\tau}{a^2 \tau_{Dx}}}} \quad (2)$$

in which A_X is the amplitude of the cross-correlation curve, τ_{Dx} is the diffusion time of the dual-labeled molecules.

Quantification of hydrodynamic radii of condensates by dcFCCS

Quantify the size of condensates. dcFCCS curves have been acquired. According to Eq. 2, dcFCCS curves are fitted to extract diffusion times (τ_{Dx}), which can be used to quantify hydrodynamic radii of heterocomplexes and condensates formed from AF488-cGAS and Cy5-dsDNA via Eq. 3[26].

$$R_{cond} = R_{dye} \times \frac{\tau_{Dx} \times Cd_{488}}{\tau_{dye}} \quad (3)$$

We used the AF488 as a standard. R_{488} is 0.58 nm[48]. The correction factor Cd_{488} was ~0.65 in our measurement, which was to calibrate diffusion times extracted from autocorrelation and cross-correlation curves and calculated according to a published procedure[24,49]. And in our experiment, relaxation time of the autocorrelation curve of AF488 under 488-nm laser excitation is ~0.09 ms.

Quantification of proportions of components participating in condensates by dcFCCS

When interactions of AF488-labeled molecules and Cy5-labeled molecules do not form condensates or oligomerization, the fraction of AF488-labeled molecules forming dual-labeled molecules can be calculated by

$$\frac{N_X}{N_{488}} = \frac{A_X}{A_{640} \times Cr_{640}} \quad (4)$$

the fraction of AF640-labeled molecules forming dual-labeled molecules can be calculated by

$$\frac{N_X}{N_{640}} = \frac{A_X}{A_{488} \times Cr_{488}} \quad (5)$$

Cr_{488} and Cr_{640} are correction factors represent the ratios of the overlapped excitation volume over the excitation volume of 488 nm laser and 640 nm laser. According to published procedure[24,26,49], correlation factors Cr_{488} and Cr_{640} were determined to be ~0.52 and ~0.64, respectively.

Quantification of binding affinities by dcFCCS

DcFCCS experiments were performed in 20 mM Tris-HCl pH 7.5, 300 mM NaCl, and 5 mM MgCl₂ at 25℃. 10 nM AF488-labeled accessory proteins were mixed with 20 nM Cy5-cGAS or 20 nM Cy5-dsDNA to quantify their binding affinities via dcFCCS. When needed, 200 nM rapamycin was added. For the light-inducible system, mixed samples were illuminated in blue light with a 1 Wm^{-2} light-emitting diode light source of 470 nm ± 20 nm before dcFCCS measurements.

Assuming that the AF488 labeled A is mixed with Cy5 labeled B to form complex A-B. According to Eq. 4, N_X/N_{488} is the proportion of AF488-A forming complex with B. Then, the binding constants can be calculated using Eq. 6.

$$A_{AF488} + B_{Cy5} \leftrightarrow AB$$

$$K_d = \frac{[A] \times [B]}{[AB]} = \frac{\left(C_A - C_A \times \frac{N_X}{N_{488}}\right) \times \left(C_B - C_A \times \frac{N_X}{N_{488}}\right)}{C_A \times \frac{N_X}{N_{488}}} \quad (6)$$

C_A and C_B are the total concentrations of AF488 labeled A and Cy5 labeled molecule, respectively. [A], [B] and [AB] are the concentrations of A_{AF488} free molecule, B_{Cy5} free molecule and A-B complex, respectively.

In vitro cGAMP synthesis assay

The cGAS and dsDNA were mixed with 1 mM ATP, 1 mM GTP in the reaction buffer (20 mM Tris-HCl pH 7.5, 100 mM NaCl, 5 mM MgCl₂) and incubated for 2 h at 37 ℃. After incubation, the samples were heated at 95 ℃ for 10 min and then centrifuged at 20,000 rpm for 10 min. The supernatant was diluted 5 folds with 20 mM Tris-HCl pH 7.5 and loaded onto a Mono QTM 5/50 column (GE Healthcare). The product was eluted with a gradient from 0 to 0.4 M NaCl in 20 mM Tris-HCl pH 7.5 at a flow rate of 0.5 mL/min. The peak of the product cGAMP was obtained at 256 nm absorbance. The software Unicorn 7.1 (GE Healthcare) was used to quantify the yield of cGAMP.

When needed, accessory proteins were incorporated at a concentration equivalent to that of cGAS. 200 nM rapamycin was included when needed. For light-inducible system, mixed samples were illuminated in blue light with a 1 Wm^{-2} light-emitting diode light source of 470 nm ± 20 nm during 2-h incubation.

In vitro phase separation of cGAS, accessory proteins and dsDNA regulated by inducible systems

The Cy5-cGAS, AF488-proteins and dsDNA were incubated for 10 min to form phase separation condensates on the coverslip (ThermoFisher

Scientific) in 5 mM Tris-HCl pH 7.5, 300 mM NaCl, 1 mM DTT. 200 nM rapamycin was included when needed. For light-inducible system, mixed samples were illuminated in blue light with a 1 W m^{-2} light-emitting diode light source of 470 nm ± 20 nm during 2-h incubation. The experiments were conducted on an AXR NSPARC (Nikon) confocal microscope using the 100×/1.42 NA oil objective. Images were captured for 30 min. The time-lapse images were processed with ImageJ.

Cell culture and plasmid transfection
HEK293T cells were cultured in Gibco-Dulbecco's modified Eagle's medium (DMEM) supplemented with 10% (v/v) fetal bovine serum (FBS), 2 mM l-glutamine, penicillin (100 U/mL), and streptomycin (100 mg/mL), and the cells were cultured in 6-well plates at 37 °C in a humidified incubator containing 5% CO_2. The cells were transfected with corresponding plasmids with the Polyethyleneimine Linear (PEI).

When rapamycin-inducible cGAS phase separation and signaling system was used, the culture medium was replaced with fresh opened DMEM supplemented with 200 nM rapamycin. When light-inducible dimerization system was used, the cells were incubated under blue light illumination source of 470 nm ± 20 nm. Cells were lysed after 48 h for the subsequent experiments.

Western blotting analysis
The HEK293T cells were lysed with radio immunoprecipitation analysis (RIPA) lysis buffer containing a protease inhibitor mixture and phosphatase inhibitor. The lysates were centrifuged at 13,000 rpm for 10 min and the supernatant was collected to measure the protein concentration by bicinchoninic acid (BCA) assay. After incubation with SDS loading buffer for 10 min at 95 °C, protein samples were resolved by 8% SDS-polyacrylamide gel electrophoresis (SDS-PAGE), transferred to a poly-vinylidene difluoride membrane, incubated with triturated saline containing 5% (w/v) milk in 0.1% Tween-20 (TBST) at 4 °C overnight, then incubated with the primary antibody for 2 h and with secondary antibody for 1 h at room temperature. Protein bands were visualized with a chemiluminescent substrate and images were acquired using an iBright 1500 imaging system. Densitometric analysis was performed using ImageJ software. All used antibody information is shown in Table S5.

RT-qPCR analysis
Cells were inoculated in six-well plates and total RNA was extracted with HiPure Total RNA Kit (MGBIO). Diluted RNA was reverse transcribed with the cDNA Synthesis Kit (ThermoFisher Scientific). The cDNA obtained from reverse transcription was used as a template for PCR amplification reaction with specific primers and PCR Master Mix (ThermoFisher Scientific). Analyzed the samples by the Quantagene q225 qPCR System (KUBO). All reagents were used according to the manufacturer's instructions. Primer sequences are listed in Table S6. GAPDH (human) was used as an internal control.

Reporting summary
Further information on research design is available in the Nature Portfolio Reporting Summary linked to this article.

Data availability
The data that support the findings of this study are in the manuscript and Supplementary Information. The numerical source data behind the graphs in the paper can be found in Supplementary Data 1. Unprocessed blot images can be found in Supplementary Data 2.

References
1. Takeuchi, O. & Akira, S. Pattern recognition receptors and inflammation. *Cell* **140**, 805–820 (2010).
2. Ablasser, A. & Chen, Z. J. cGAS in action: expanding roles in immunity and inflammation. *Science* **363** (2019).
3. Hong, Y. et al. Janus kinase inhibition for autoinflammation in patients with DNASE2 deficiency. *J. Allergy Clin. Immunol.* **145**, 701–705.e8 (2020).
4. Motwani, M., Pesiridis, S. & Fitzgerald, K. A. DNA sensing by the cGAS–STING pathway in health and disease. *Nat. Rev. Genet.* **20**, 657–674 (2019).
5. Chen, C. & Xu, P. Cellular functions of cGAS-STING signaling. *Trends Cell Biol.* **33**, 630–648 (2023).
6. Ablasser, A. et al. cGAS produces a 2′-5′-linked cyclic dinucleotide second messenger that activates STING. *Nature* **498**, 380–384 (2013).
7. Kranzusch, P. J. & Vance, R. E. cGAS dimerization entangles DNA recognition. *Immunity* **39**, 992–994 (2013).
8. Pathare, G. R. et al. Structural mechanism of cGAS inhibition by the nucleosome. *Nature* **587**, 668–672 (2020).
9. Kranzusch, P. J., Lee, A. S., Berger, J. M. & Doudna, J. A. Structure of human cGAS reveals a conserved family of second-messenger enzymes in innate immunity. *Cell Rep.* **3**, 1362–1368 (2013).
10. Zhang, X. et al. The cytosolic DNA sensor cGAS forms an oligomeric complex with DNA and undergoes switch-like conformational changes in the activation loop. *Cell Rep.* **6**, 421–430 (2014).
11. Diner, E. J. et al. The innate immune DNA Sensor cGAS produces a noncanonical cyclic dinucleotide that activates human STING. *Cell Rep.* **3**, 1355–1361 (2013).
12. Xie, W. et al. Human cGAS catalytic domain has an additional DNA-binding interface that enhances enzymatic activity and liquid-phase condensation. *Proc. Natl Acad. Sci.* **116**, 11946–11955 (2019).
13. Du, M. & Chen, Z. J. DNA-induced liquid phase condensation of cGAS activates innate immune signaling. *Science* **361**, 704–709 (2018).
14. Zhou, W., Mohr, L., Maciejowski, J. & Kranzusch, P. J. cGAS phase separation inhibits TREX1-mediated DNA degradation and enhances cytosolic DNA sensing. *Mol. Cell* **81**, 739–755.e7 (2021).
15. Hertzog, J. & Rehwinkel, J. Regulation and inhibition of the DNA sensor cGAS. *EMBO Rep.* **21** (2020).
16. Liao, C.-Y., Lei, C.-Q. & Shu, H.-B. PCBP1 modulates the innate immune response by facilitating the binding of cGAS to DNA. *Cell. Mol. Immunol.* **18**, 2334–2343 (2020).
17. Liu, Z.-S. et al. G3BP1 promotes DNA binding and activation of cGAS. *Nat. Immunol.* **20**, 18–28 (2018).
18. Zhao, M. et al. The stress granule protein G3BP1 promotes pre-condensation of cGAS to allow rapid responses to DNA. *EMBO Rep.* **23** (2021).
19. Xu, G. et al. Viral tegument proteins restrict cGAS-DNA phase separation to mediate immune evasion. *Mol. Cell* **81**, 2823–2837.e9 (2021).
20. Hertzog, J. et al. Varicella-Zoster virus ORF9 is an antagonist of the DNA sensor cGAS. *EMBO J.* **41** (2022).
21. Bhowmik, D. et al. Cooperative DNA binding mediated by KicGAS/ORF52 oligomerization allows inhibition of DNA-induced phase separation and activation of cGAS. *Nucleic Acids Res.* **49**, 9389–9403 (2021).
22. Huang, J. et al. Herpes simplex virus 1 tegument protein VP22 abrogates cGAS/STING-mediated antiviral innate immunity. *J. Virol.* **92** (2018).
23. Wu, J.-j. et al. Inhibition of cGAS DNA Sensing by a Herpesvirus Virion Protein. *Cell Host Microbe* **18**, 333–344 (2015).
24. Peng, S. et al. Phase separation at the nanoscale quantified by dcFCCS. *Proc. Natl Acad. Sci.* **117**, 27124–27131 (2020).
25. Yao, Y., Wang, W., Chen, C. & Hiller, K. Mechanisms of phase-separation-mediated cGAS activation revealed by dcFCCS. *PNAS Nexus* **1** (2022).
26. Yao, Y., Wang, W. & Chen, C. Quantifying phase separation at the nanoscale by dual-color fluorescence cross-correlation spectroscopy (dcFCCS). *Biophys. Rep.* **8**, 29–41 (2022).

27. Brangwynne, C. P., Mitchison, T. J. & Hyman, A. A. Active liquid-like behavior of nucleoli determines their size and shape in oocytes. *Proc. Natl Acad. Sci. USA* **108**, 4334–4339 (2011).

28. Nihongaki, Y., Otabe, T., Ueda, Y. & Sato, M. A split CRISPR–Cpf1 platform for inducible genome editing and gene activation. *Nat. Chem. Biol.* **15**, 882–888 (2019).

29. DeRose, R., Miyamoto, T. & Inoue, T. Manipulating signaling at will: chemically-inducible dimerization (CID) techniques resolve problems in cell biology. *Pflügers Arch. Eur. J. Physiol.* **465**, 409–417 (2013).

30. Inobe, T. & Nukina, N. Rapamycin-induced oligomer formation system of FRB–FKBP fusion proteins. *J. Biosci. Bioeng.* **122**, 40–46 (2016).

31. Kawano, F., Suzuki, H., Furuya, A. & Sato, M. Engineered pairs of distinct photoswitches for optogenetic control of cellular proteins. *Nat. Commun.* **6** (2015).

32. Li, P. et al. Phase transitions in the assembly of multivalent signalling proteins. *Nature* **483**, 336–340 (2012).

33. Chen, S., Rong, M., Lv, Y., Zhu, D. & Xiang, Y. Regulation of cGAS activity by RNA-modulated phase separation. *EMBO Rep.* **24** (2022).

34. Banani, S. F., Lee, H. O., Hyman, A. A. & Rosen, M. K. Biomolecular condensates: organizers of cellular biochemistry. *Nat. Rev. Mol. Cell Biol.* **18**, 285–298 (2017).

35. Shin, Y. et al. Spatiotemporal control of intracellular phase transitions using light-activated optodroplets. *Cell* **168**, 159–171.e14 (2017).

36. Taslimi, A. et al. An optimized optogenetic clustering tool for probing protein interaction and function. *Nat. Commun.* **5** (2014).

37. Hong, K., Song, D. & Jung, Y. Behavior control of membrane-less protein liquid condensates with metal ion-induced phase separation. *Nat. Commun.* **11** (2020).

38. Nakamura, H. et al. Intracellular production of hydrogels and synthetic RNA granules by multivalent molecular interactions. *Nat. Mater.* **17**, 79–89 (2017).

39. Hernandez-Candia, C. N., Brady, B. R., Harrison, E. & Tucker, C. L. A platform to induce and mature biomolecular condensates using chemicals and light. *Nat. Chem. Biol.* (2024).

40. Bracha, D. et al. Mapping local and global liquid phase behavior in living cells using photo-oligomerizable seeds. *Cell* **175**, 1467–1480.e13 (2018).

41. Kim, Y. J. et al. Light-activated macromolecular phase separation modulates transcription by reconfiguring chromatin interactions. *Sci. Adv.* **9** (2023).

42. Lian, H. et al. ZCCHC3 is a co-sensor of cGAS for dsDNA recognition in innate immune response. *Nat. Commun.* **9** (2018).

43. Yoh, S. M. et al. PQBP1 is a proximal sensor of the cGAS-dependent innate response to HIV-1. *Cell* **161**, 1293–1305 (2015).

44. Huang, Z.-F. et al. Human cytomegalovirus protein UL31 inhibits DNA sensing of cGAS to mediate immune evasion. *Cell Host Microbe* **24**, 69–80.e4 (2018).

45. DeFilippis, V. R. et al. Human cytomegalovirus protein UL42 antagonizes cGAS/MITA-mediated innate antiviral response. *PLOS Pathog.* **15** (2019).

46. Zavaliev, R., Mohan, R., Chen, T. & Dong, X. Formation of NPR1 condensates promotes cell survival during the plant immune response. *Cell* **182**, 1093–1108.e18 (2020).

47. Gallego, L. D. et al. Phase separation directs ubiquitination of gene-body nucleosomes. *Nature* **579**, 592–597 (2020).

48. Heyman, N. S. & Burt, J. M. Hindered diffusion through an aqueous pore describes invariant dye selectivity of Cx43 junctions. *Biophys. J.* **94**, 840–854 (2008).

49. Werner, S., Ebenhan, J., Haupt, C. & Bacia, K. A quantitative and reliable calibration standard for dual-color fluorescence cross-correlation spectroscopy. *ChemPhysChem* **19**, 3436–3444 (2018).

Author contributions
C.C. conceived and supervised the project; Y.T. prepared materials and performed experiments with help from W.W., and Y.T. and C.C. wrote the paper.

Competing interests
The authors declare no competing interests.

Additional information
Supplementary information The online version contains supplementary material available at https://doi.org/10.1038/s42003-025-07892-5.

Correspondence and requests for materials should be addressed to Chunlai Chen.

Peer review information *Communications Biology* thanks the anonymous reviewers for their contribution to the peer review of this work. Primary Handling Editors: Huan Bao and Mengtan Xing.

Reprints and permissions information is available at http://www.nature.com/reprints

Publisher's note Springer Nature remains neutral with regard to jurisdictional claims in published maps and institutional affiliations.